

Salinity induced stiffening of drying particulate film and dynamic warping

Hisayama ^{1,*}, Ludovic Pauchard,^{2,†} Frédérique Giorgiutti-Dauphine,² and Sanjoy Khawas ³

¹*Department of Physics, The University of Tokyo, 7-3-1 Hongo, Bunkyo-Ku, Tokyo 113-0033, Japan*

²*Université Paris-Saclay, CNRS, FAST, F-91405 Orsay, France*

³*Department of Physics, Indian Institute of Technology Bombay, Powai, Mumbai 400076, India*



(Received 14 September 2022; revised 24 January 2023; accepted 1 February 2023; published 27 February 2023)

When the particle dispersion is dried, its constituents consolidate to form a solid particulate film, resulting in a transition from a liquid to a solid phase. The resultant particulate film stores the strain energy, which builds up during its formation and is often released to crack and warp. Here, we investigate the dependence of ionic strength of dispersion on the mechanical property of a resultant dried particulate film in conjunction with their role in warping. We show that the increasing ionic strength results in a faster consolidation of its constituents, increasing interparticle adhesion, thereby changing the particulate film's Young's modulus and limiting the drying induced warping. We explain this phenomenon using a theoretical model, wherein we show that the differential shrinkage during the drying in the particulate film generates the strain gradient, which later results in warping. Furthermore, our calculation shows that the curvature of a warped region is proportional to the strain gradient and is inversely proportional to the particulate film's Young's modulus.

DOI: [10.1103/PhysRevMaterials.7.025604](https://doi.org/10.1103/PhysRevMaterials.7.025604)

I. INTRODUCTION

Drying particle dispersion and its transformation into a particulate film is a complex physical process wherein the constituting particles consolidate due to fluid evaporation [1–5]. The evaporation induced drying is considered one of the amenable methods to obtain a particulate film or functional coatings [1,2,4]. However, the particulate films often accompany mechanical defects such as cracks, debonding, and warping, which result in material failure [2,6–10]. Interestingly, such defects are also seen at geological length scales, e.g., mud cracks and warping on the dried river bed [11,12]. The formation of particulate film and the mechanical defects depend on several parameters: physicochemical condition [7,13], shape [5] and size of constituting entities [14], evaporation kinetics [3,15], etc. In principle, the defects nucleate due to the release of excess strain energy that accumulates during the drying. This strain energy develops during the evaporation induced consolidation of particles [12,16,17]. From Griffith's criterion, releasing excess strain energy equals the energy essential for creating new surfaces through defect nucleation. For example, during the formation of cracks, the energy released is equal to twice the surface free energy (associated with newly created surfaces) [17], and its equivalent to the sum of adhesion energy and bending energy for warpings.

The particulate film has several technological applications and is realized in various forms, such as the coating on electrodes [18], colloidal crystals and paintings, etc. [1–5]. Over the past few decades, the research on drying induced cracks and their manifestation into different morphological forms

has gained much attention [12]. More focus was on crack morphology and their evolution as a function of constituting particles' shape and size, physicochemical condition and salinity, etc. [3]. The mechanical properties of a particulate film play a significant role in the nucleation of mechanical defects. For example, warping in the particulate film varies with the film's Young's modulus [19–21]. As a result, the particulate film tends to bend if the film is stiff, while it does not bend when it is soft. For practical applications, the particulate film should be defect free, i.e., they should not crack or warp. Consequently, developing a new design principle is essential, and it requires an in-depth understanding of the phenomenon under different experimental conditions. For such purposes, varying the physicochemical aspect can be helpful, as it is one of the control parameters that can modulate the evaporation induced consolidation process, which could further affect the film's mechanical integrity and therefore the resulting defects. Here, in this paper, we investigate the role of physicochemical aspects on particulate film by altering the ionic concentration I in the aqueous phase. On adding NaCl salt in an aqueous phase of dispersion, the ionic charges adsorbed onto the surface of the particles are screened, resulting in a variation in I , which further introduces the attractive interaction between the constituents and creates faster consolidation [13]. Furthermore, it modulates the mechanical properties of a resultant particulate film. Consequently, we observe that the Young's modulus of a dried particulate film increases, i.e., the film gets stiffer. In addition, the particulate film warps, which persists at low salt concentrations and gets suppressed at a higher NaCl concentration. We explain our observation by a simple model which shows that the differential shrinkage induced strain gradient plays a crucial role in the bending of the particulate film and generation of warping. In addition, our calculation shows the intricate correlation between the curvature of a

*hisayama@noneq.phys.s.u-tokyo.ac.jp

†ludovic.pauchard@universite-paris-saclay.fr

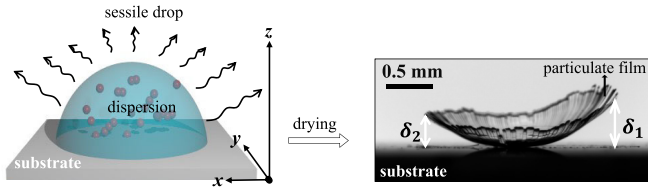


FIG. 1. Left: The schematic depicts the sessile drop evaporation. Right: Side view of dried particulate films formed after the evaporation of fluid from the sessile drop. The marked symbols, δ_1 and δ_2 , refer to the deflection of the left and right sides of the warped particulate film.

warped particulate film, the strain gradient, and the particulate film’s Young’s modulus.

II. MATERIALS AND METHODS

A. Drying experiments

We perform sessile drop drying experiments to investigate the particulate film’s mechanical properties and drying induced warping (as shown in Fig. 1). Here, the drying dispersion comprises silica particles commercially known as Ludox HS-40 (Sigma Aldrich, USA), with the diameter of the constituting particles being $a = 12$ nm and the surface area of 220 m²/g. The pH of stock dispersion is 9.8. In the present study, we perform experiments at various particle concentrations, $\phi \in [2 \text{ wt } \%, 40 \text{ wt } \%]$, obtained by diluting the stock dispersion with milli-Q water (resistivity of 18.2 M Ω cm). The ionic strength I of dispersion is varied between 0.01 and 0.5 mol/L by adding NaCl salt. For experimentation, we choose microscope glass slides as a substrate. These glass slides are sonicated for 30 min, washed with the soap solution, cleaned with milli-Q water, and dried with dry N₂ gas. The contact angle θ_c of water on these glass slides is estimated to be $16 \pm 2^\circ$. In typical experiments, we place a drop of specific volume 10 μ L on a substrate and then investigate the formation of drying induced warping. The droplet was then allowed to dry at an ambient atmosphere with temperature $T = 25 \pm 2^\circ\text{C}$ and relative humidity $\text{RH} = 40 \pm 5\%$. Under these conditions (absence of convection in the vapor), the water molecules transfer into the atmosphere through diffusion. For monitoring the drying kinetics, we use a home-built, long-working distance microscope comprising a telescopic lens (from Optem, USA) and a variable objective ($2\times$ – $10\times$). In addition, an IDS camera integrated into the droplet shape analyzer (DSA 25S from Kruss GmbH, Germany) captures the colloidal dispersion’s drying and warping dynamics.

B. Rheological characterization

The rheological measurements of colloidal dispersions are performed with an imposed shear rate rheometer (Contraves Low Shear LS30) equipped with a concentric-cylinder Couette type. For the rheological study, we first prepare the colloidal dispersion with a specific NaCl content by mixing NaCl with a vortex stirrer for 30 s. Then, we load the dispersion into the sample cell for testing. Finally, we measure the viscosity in the absence of evaporation. Note that here, to prevent evaporation, we cover the sample cell with a wet sponge

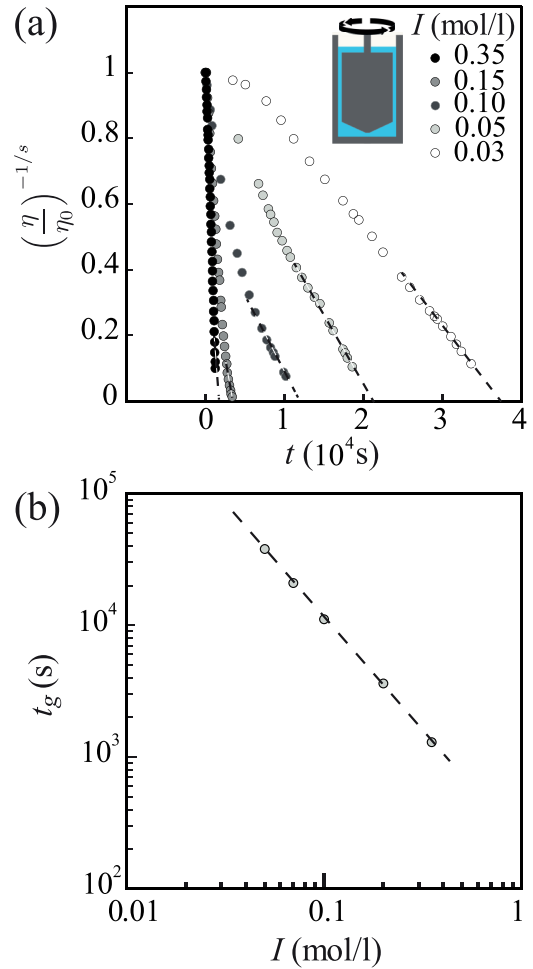


FIG. 2. (a) Dimensionless viscosity $(\eta/\eta_0)^{-1/s}$ vs time for HS40 dispersions exhibiting different ionic strengths I (η_0 is the initial viscosity of the dispersion). The exponent s is chosen to fit the measurements along a straight line when $t \rightarrow t_g$ ($s = 1.6$). (b) The resulting gelation time is plotted as a function of the ionic strength in a log-log scale.

cap. The experiments are performed at a constant shear rate of 0.3 or 3 s^{−1}, respectively. Interestingly, both shear rates give similar results. We present here only the results with 3 s^{−1} as shown in Fig. 2(a). Our measurements reveal that in the absence of evaporation, the viscosity of salty dispersion increases first slowly and then diverges. We understand the temporal variation of the viscosity using a scalar percolation model of the sol-gel transition [22] following the equation

$$\eta \propto \frac{\eta_0}{(t_g - t)^s}, \quad (1)$$

where s is a characteristic exponent. In agreement with the percolation theory, Eq. (1) is valid for t close to t_g . Hence, for each series of dots in Fig. 2(a), the value of s is determined to obtain an alignment of the values corresponding to $(\eta/\eta_0)^{-1/s}$ on a line in the vicinity of $t = t_g$. The resulting gelation time t_g exponentially decreases with the ionic strength I of the dispersion [as shown in Fig. 2(b)], which directly implies that the dispersion with a higher NaCl content results in a relatively faster consolidation. Note that in the presence of

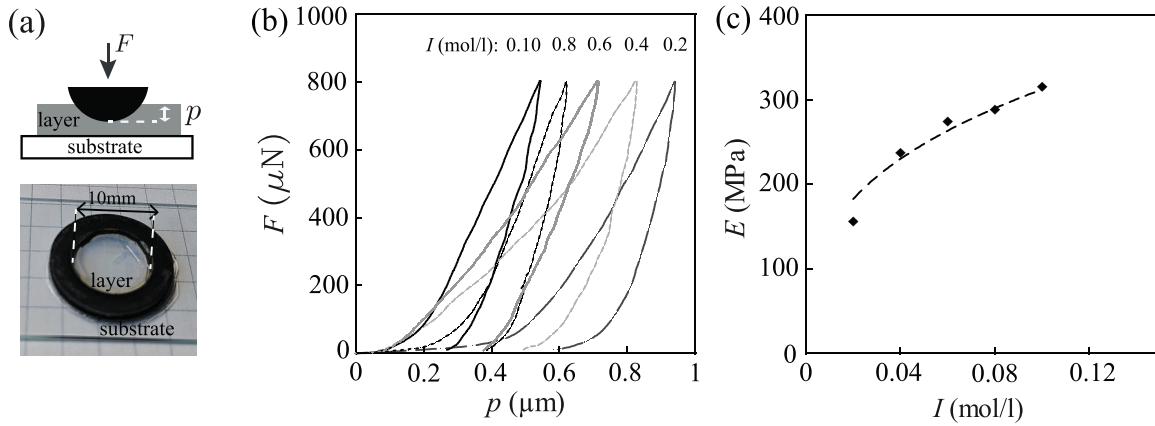


FIG. 3. Mechanical characterisation using indentation testing in the geometry sketched in side view and imaged in (a). (b) Spherical indentation load displacement showing load-unload curves (applied force F vs penetration depth p). The Young's modulus value is derived from the slope of the unloading part at the maximum load; the dashed line represents a guide for the eye for the best fits of the slope of the initial unloading for the case $I = 0.03$ mol/l. (c) Plot of Young's moduli as a function of the film ionic strength from the Oliver-Pharr method. The dashed lines correspond to the scaling law from equation (5).

evaporation induced drying, the consolidation time depends on another additional timescale, namely, the evaporation time.

C. Mechanical characterization

The elastic moduli of the solid particulate films with various ionic strengths are measured using the indentation test (Bio-indenter from Anton Paar). We use a spherical tip as an indenter of radius $R = 0.25$ mm (the tip is assumed perfectly rigid) [15]. We indent the sample with a fixed loading speed of 100 mN/min and then measured the penetration depth p as a function of the applied force F . Our testing specimen (the particulate film) is a planar dried film adhering to a rigid substrate (glass microscope slide), as shown in Fig. 3(a). The thickness of the dried films, close to 200 μm , is at least 10 times larger than the maximum value of the penetration depth of the indenter, limiting the influence of the substrate on the measurements. Note that the film considered for the indentation characterization is much thicker than the warped film. We typically perform mechanical testing a few minutes after the formation of the cracking network; this avoids the formation of cracks due to the contact of an indenter tip during the measurement. It is worth mentioning that testing specimens do not warp during the indentation experiment.

We extract the elastic properties of materials from the unloading part of data using the Oliver-Pharr model [23,24]. Figure 3(b) shows the indentation force versus penetration depth on particulate films with different ionic strengths. The stiffness and therefore Young's modulus of a solid film is measured from the slope at the initial unloading curve,

$$\left. \frac{dF_{\max}}{dp} \right|_{p_{\max}} = \frac{2}{\sqrt{\pi}} \frac{E_r}{(1-\nu^2)} \sqrt{A_p}, \quad (2)$$

where E_r is the reduced Young's modulus, p_{\max} is the maximum displacement when the indenter is fully loaded, F_{\max} is the maximum load at p_{\max} , and $A_p = \pi p_{\max}(2R - p_{\max})$ is the projected circular area of the contact for the sphere

indenter into a half space by a distance $p = p_{\max}$. The Young's modulus E is derived from the reduced Young's modulus [23].

III. RESULTS

A. Particulate film's mechanical properties and dependence on ionic strength

The Young's moduli of particulate films are plotted as a function of the ionic strength in Fig. 3(c). As shown in Fig. 3(c), the Young's moduli of particulate films increase with increasing the content of NaCl in the film. This infers that the addition of NaCl stiffens the dried particulate film. We hypothesize that the stiffening of the particulate film is due to the strengthening of the interparticle attractive interaction between the silica particles [25]. From a macroscopic point of view, the Young's modulus E of the particle assembly constituting the particulate film depends on the adhesion energy between particles. If the adhesion energy between silica particles is noted W_0 without NaCl, then the increased adhesion energy in the presence of NaCl, $W = W_0 + W(I)$. The reason for such an increase in the adhesion energy is related to the ionic bonding between particles. The Young's modulus in terms of adhesion energy is expressed as [26]

$$E \propto \phi^4 (E_0^2 W/a)^{1/3}, \quad (3)$$

where E_0 is the Young's modulus of the particle material and ϕ is the volume fraction. Assuming the linear dependence between W and I , i.e., $W \sim I$. We perform a polynomial fitting to the plot showing the variation in the Young's modulus of a particulate film versus I as shown in Fig. 3(b). The estimated magnitude of E fits well with the scaling law expressed below,

$$E \propto I^{1/3}. \quad (4)$$

Therefore, the Young's modulus E increases nonlinearly with I , also inferring a nonlinear increase in adhesion energy W between the particles with the exponent being 1/3 or 0.33 approximately.

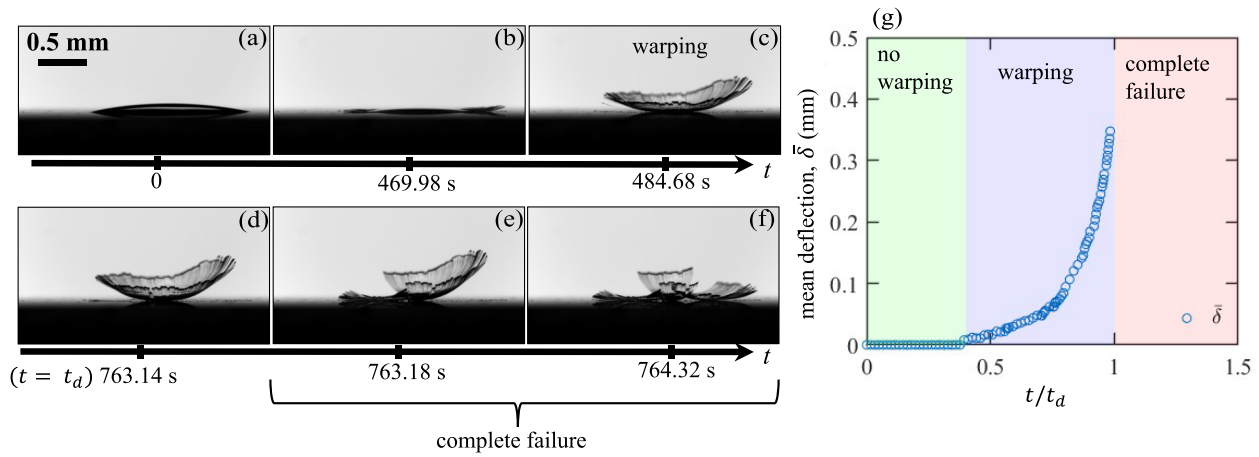


FIG. 4. (a)–(f) Snapshots of drying sessile drop at different times, t varying from 0 to 764.32 s. As time elapses, the particulate film bends, warping with increasing deflection amplitude δ . The desiccation time t_d is when fluid completely evaporates and the curling process completes. At $t > t_d$, the particulate film completely fails, with films getting fragmented into pieces. (g) The plot of mean deflection $\bar{\delta} = (\delta_1 + \delta_2)/2$ vs the scaled time t/t_d . There are different regions, green, purple and pink, representing the different physical states of drying particulate film: (i) no warping (green region), (ii) warping or bending of the particulate film (purple region), and (iii) complete failure, representing the fragmentation (pink region).

B. Warping of a particulate film

In this section, we illustrate the morphological changes in the drying dispersion (sessile drop) that consist of silica particles (10 wt %) as a function of drying time. In Figs. 4(a)–4(f), we present the images showing the side view of a drying droplet. It shows the transition from a state of a liquid drop to a particulate film. The images in Figs. 4(a)–4(f) are taken at different times t . As the liquid evaporates, the dispersion solidifies to form a semisolid particulate film which originates from the evaporation induced consolidation of silica particles. The solidification initially starts from the droplet edge and then propagates towards the interior of a drop (between $t = 0$ and 763.14 s). The drying particulate film accompanies mechanical instabilities, namely, warping that occurs from the droplet edge and proceeds to the interior [shown in Figs. 4(b)–4(d)]. Finally, at the tail end of drying at 763.18 s, the particulate film breaks into fragments as shown in Figs. 4(e) and 4(f). During drying, the particulate film’s edge continuously bends, resulting in its upward curling (warping) in a nearly symmetric manner. It continues until the film completely dries and fragments. From the side view, the particulate film appears as a thin rectangular beam that bends from both sides (left and right), resulting in its deflection δ_1 and δ_2 on the left and right sides, respectively. We quantitatively characterize the warping process by estimating the magnitude of the mean deflection $\bar{\delta} (= \frac{\delta_1 + \delta_2}{2})$ as a function of drying time. The plot showing the variation in $\bar{\delta}$ with scaled time t/t_d , where t_d is the desiccation time = 763.14 s is shown in Fig. 4(g). The magnitude of deflection of a drying particulate film increases nonlinearly as a function of t/t_d until it fragments. Based on the physical state of a drying particulate film, we classify them as (i) no warping, (ii) warping, (iii) complete failure. The “no-warping” regime corresponds to the region where the film does not curl, the “warping” is a regime where the film curls, and “complete failure” corresponds to the region where the film fragments into pieces.

Next, on drying a particle dispersion in a fixed environmental condition but with varying salinity, i.e., at different molar concentrations I (in mol/L) of NaCl, we observe the variation in its warping. We monitor the sessile drop drying experiments with colloidal dispersions at different NaCl concentrations I (in mol/L) with a primary focus on their structural evolution and transformation from a liquid to a dried particulate film. In Figs. 5(a)–5(d) and Figs. 5(e)–5(h) we show the side view and top view of the dried particulate film at various ionic concentrations, $I \in [0, 0.06]$ mol/L, respectively. The side view of the dried particulate films (just before fragmentation) with different I shows that the particulate film detaches from the initial pinning point (droplet edge), while the top view of the particulate films shown in Figs. 5(e)–5(h) displays that the warping accompanies radial cracks. Furthermore, we noted that the mean crack spacing (averaged over length) in the particulate film increases from 42 ± 12 to $\sim 72 \pm 33$ μm on increasing I from 0 to 0.04 mol/L, and then at 0.06 mol/L it decreases to 55 ± 23 μm . However, the spatial fluctuation in the magnitude of crack spacing is quite large; therefore, it is hard to infer anything from a quantitative analysis. Such subtle differences in mean crack spacing at $I = 0.04$ and 0.06 mol/L can occur due to the fluctuation in experimental conditions. Irrespective of I , the crack pattern remains unaltered. From Figs. 5(a) and 5(c), it is obvious that at $I = 0$ and 0.04 mol/L, the dried particulate film warps and curls upward, while as the NaCl content in the drying dispersion increases, the magnitude of $\bar{\delta}_{\text{max}}$ reduces, and at $I > 0.06$ mol/L, the particulate film does not bend at all, i.e., no upward curling. Further, to better visualize the warping dynamics and understand the process, we plot the instantaneous mean deflection $\bar{\delta}$ for a given I (in mol/L) as a function of scaled desiccation time t/t_d as shown in Fig. 6. As earlier, we again observe that the magnitude of deflection of the warped particulate film increases nonlinearly with time. However, increasing I slows down deflection and even suppresses the warping. Figure 6 shows that warping ceases when I exceeds 0.06 mol/L.

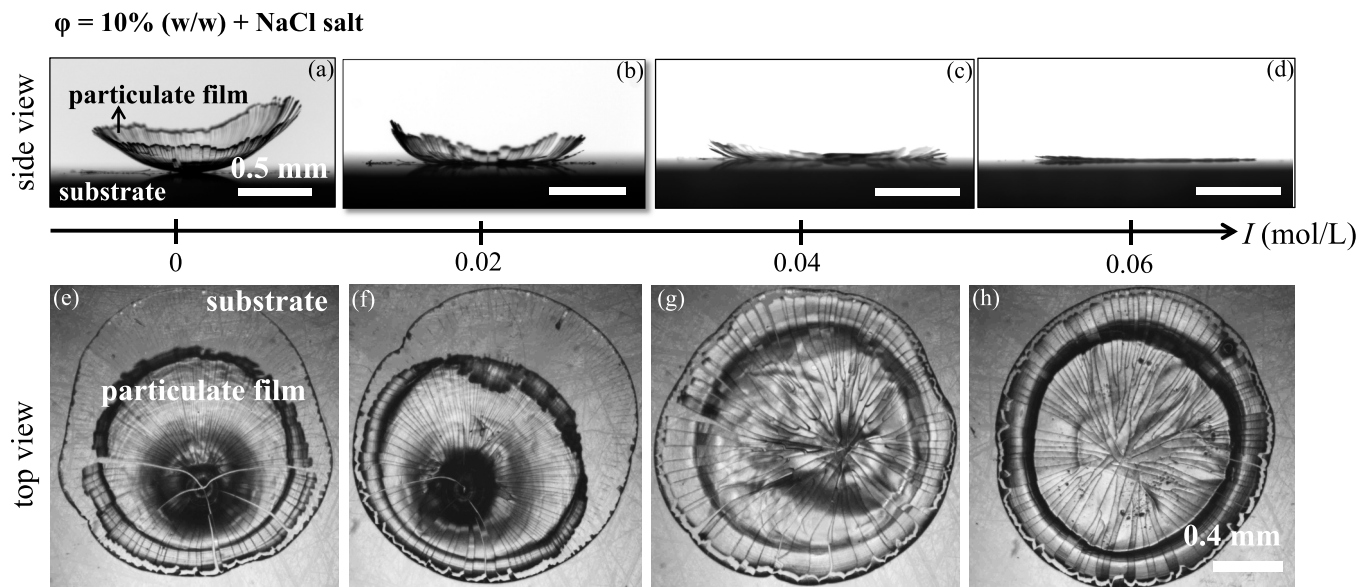


FIG. 5. (a)–(d) Images of the side view of dried particulate films (before complete failure) at a specific NaCl salt concentration I in mol/L, respectively. The initial concentration of dispersion is around 10 wt %. The warping varies as a function of I , and suppresses at $I = 0.06$ mol/L. (e), (f) Images of the top view of the dried particulate films (before complete failure). The dried films exhibit radial cracks and warping. The film detaches from the initial pinning point at $I = 0$ – 0.04 mol/L while it remains intact for 0.06 mol/L.

C. Debonding versus warping

Here, we discuss drying the particulate film to a substrate adhesion [Figs. 7(a) and 7(b)]. The adhesion between the particulate film and substrate persists as long as the stored strain energy does not exceed the adhesion energy. The capillary forces are known to play a significant role in such adhesion [27]. The long-range attractive capillary forces are usually larger than the other relevant short-range interactions such as the van der Waals attraction or chemical siloxane bonding at the particle contacts. When the stored strain en-

ergy overcomes the adhesion energy, debonding and warping of the colloidal deposits occur. The debonding and warping depend on the porous film’s ability to deform. In particular, the semisolid deposit, as depicted in Fig. 7(b), is the region of the deformable film in which mechanical stress develops. The physicochemical properties, particularly the salinity considered in this paper, strongly affect the mechanical properties of such semisolid deposits. Here, we perform a separate sessile drop drying experiment to investigate the debonding of the particulate film with and without NaCl. In either situation, radial cracks propagate and follow a solidification front, as shown in Fig. 8. Furthermore, it is apparent from the inter-

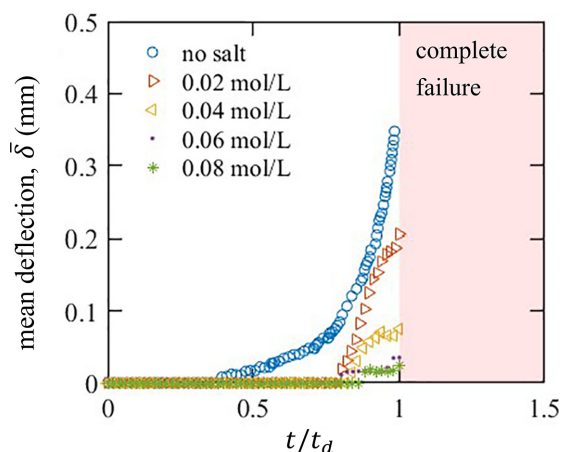


FIG. 6. The plot of mean deflection $\bar{\delta} = (\delta_1 + \delta_2)/2$ vs the scaled time t/t_d for the particulate film with no NaCl and varying NaCl concentrations $I = 0.02, 0.04, 0.06, 0.08$ mol/L, respectively. The δ varies nonlinearly with the scaled time. With an increasing concentration of NaCl, the deflection process slows down. The particulate film does not bend when $I = 0.08$ mol/L. The pink region refers to the complete failure wherein the particulate film is fragmented.

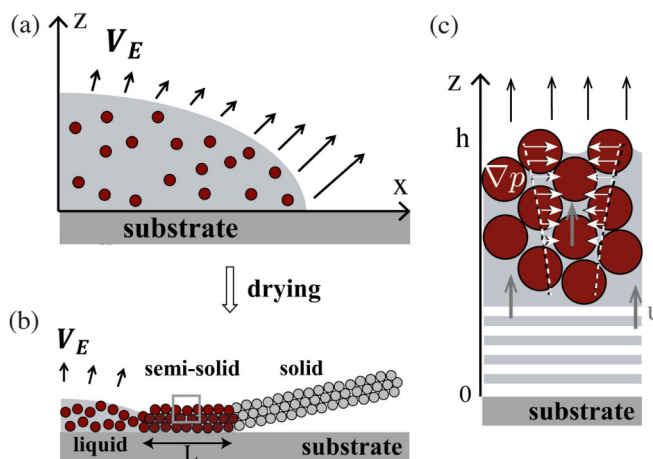


FIG. 7. (a) Drying of a sessile colloidal drop. (b) The transport of solvent drives the particles at the drop edge. A semisolid or “soft solid” is formed in which drying stress develop. (c) Sketch of the pressure gradient induced by the drying in a region of the semisolid film outlined in gray in the sketch (b).

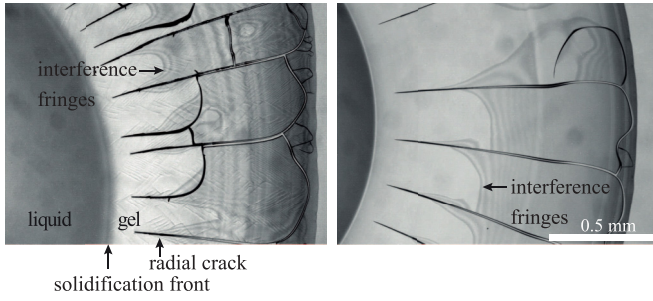


FIG. 8. Crack pattern on the edge of a sessile drop for a Ludox HS40 dispersion without NaCl salt (left) and with NaCl salt (right); images were taken at the same time after drop deposition. The optical interference fringes display an air gap between the gel and the substrate, indicating debonding. Faster consolidation is observed in the presence of NaCl salt.

ference fringes (in Fig. 8) displaying an air gap between the film and the substrate that, regardless of the amount of NaCl, debonding of the gel always occurs. Though the presence of NaCl in the dispersion significantly alters the drying kinetics, stiffening the film and preventing warping, it still could not avert the film substrate de-adhesion. Therefore, the presence of NaCl in the dispersion could not prevent debonding, despite the stiffening of the film. We also like to highlight that adhesion strength between the substrate and the particulate film impacts debonding as the critical stress for debonding directly depends on the interfacial energy per unit area. The stronger adhesion of a particulate film with the substrate resists its detachment from the substrate and might delay its debonding and therefore the warping. However, the bending curvature of the particulate film should not be affected by the adhesion as it is independent of film-substrate adhesion.

IV. DISCUSSION

This section presents a possible mechanism that supports our experimental finding on variation in warping magnitude as a function of the ionic strength. When a sessile drop of colloidal dispersion evaporates, a gelled foot builds up near the three-phase line due to the “coffee ring” effect [28]. In this semisolid gel, the drying stress develops, and the radial cracks resemble a “petals” form. Each of these petals is similar to long strips of drying gel (Fig. 8). These strips dry directionally along the length, along the x axis, and along the thickness, the z axis (vertical) (depicted in Fig. 7). In this way, we analyze the strain gradients that develop during the drying in the semisolid particulate film akin to a gel-like phase [Fig. 7(b)]. This semisolid drying film is analogous to a rectangular segment that bends with positive curvature. Assuming a homogeneous isotropic poroelastic layer of thickness h saturated with liquid, a linear poroelastic constitutive relates the mechanical stress σ_{ij} on the porous structure and the strain ϵ_{ij} as [11]

$$\sigma_{ij} = \frac{1-2\nu}{1-\nu} \alpha (p_0 - p) \delta_{ij}, \quad (5)$$

where α is the Biot-Willis coefficient, p_0 is the initial pressure when there is no stress on an unstrained structure, and p is the

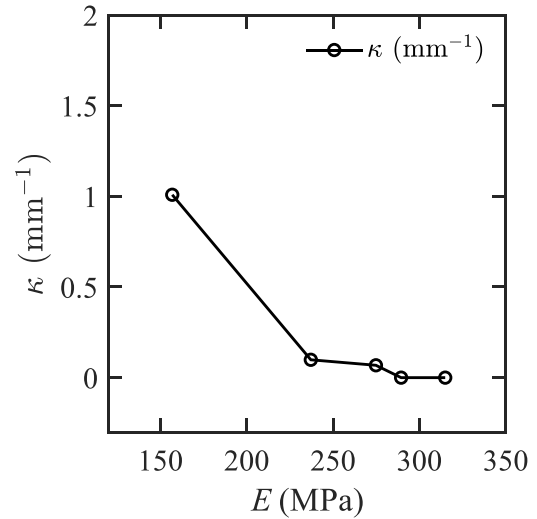


FIG. 9. Plot of maximum curvature κ of a warped particulate film of different Young’s modulus E (obtained from Fig. 3). The maximum curvature κ is the curvature estimated just before the complete failure of a particulate film.

liquid pressure in the pores of the structure. Equation (5) gives the in-plane stress $\sigma_{xx} = \sigma_{yy}$ in the plane, assuming the planar geometry of film results $\sigma_{zz} \ll \sigma_{xx}$.

Drying a particulate film causes an incompressible flow in the porous medium. The Darcy model can describe this flow, as it provides a linear relationship between pressure gradient ∇p and flow rate u [22]: The liquid water flux is driven by a liquid pressure gradient accordingly with the Darcy law [22],

$$u = \frac{k}{\eta_s} \nabla p. \quad (6)$$

This equation highlights that a pressure gradient drives the flow of liquid with viscosity η_s through a porous medium of permeability k as Fig. 7(c). At the surface Eq. (6) can be written as

$$V_E = \frac{k}{\eta_s} \nabla_z p \Big|_{z=h}, \quad (7)$$

where V_E is the constant evaporation rate. For the planar geometry of a particulate film, Eqs. (5) and (7) allow us to express the strain gradient in the plane of the film as a function of the physical properties of the gel:

$$\nabla \epsilon_{xx} \Big|_{z=h} = \frac{\eta_s V_E}{E k}. \quad (8)$$

ϵ_{xx} acts as the bending strain related to the reference strain ϵ_0 at the bottom of the film and is expressed as

$$\epsilon_{xx} = \epsilon_0 - \kappa z, \quad (9)$$

where κ is the curvature of the strip. Using Eq. (8), κ can be shown proportional to the curvature of the particulate film:

$$\kappa \propto \frac{\eta_s V_E}{E k}. \quad (10)$$

To support the validity of Eq. (10), we plot the maximum curvature κ of a warped particulate film of different Young’s modulus E (shown in Fig. 9). The maximum curvature κ is the

magnitude attained by a warping particulate film just before its complete failure. It is apparent from these figures that the κ is inversely proportional to the Young's modulus.

This simple empirical relation shows that a differential shrinkage can cause the gel to peel or warp due to the strain gradient $\nabla_z \epsilon_{xx}$. Moreover, at a constant evaporation rate, on increasing E , $\nabla_z \epsilon_{xx}$ and κ decrease. Referring to our experimental observations, the addition of NaCl content in the dispersion results in an increase of the Young's modulus E of the particulate film, while the strain gradient reduces [29]. As a result, the curvature of the particulate film reduces; therefore, there is a decrease in warping magnitude with increasing ionic strength.

V. CONCLUSION

To summarize, we report the stiffening of a dried particulate film with the increase in ionic strength I of a drying dispersion and investigate the particulate film's warping dynamics as a function of NaCl content. Our experiments reveal that the increasing NaCl concentration increases the Young's modulus of the resultant dried particulate film. We attribute such stiffening in the presence of NaCl to the strong interparticle adhesion between the constituting particles. In addition,

the particulate film warps with the mean deflection of a warped region at the tail end of the drying decreasing with increasing NaCl concentration. Further increasing NaCl limits the warping in the particulate film. We support our experimental observation with a theoretical model wherein we consider the drying particulate film a poroelastic solid that undergoes shrinkage during drying. The shrinkage of drying particulate film generates the strain gradient across the film, further resulting in its warping. Finally, we empirically show that the curvature of the warped region is proportional to the strain gradient and inversely proportional to the Young's modulus of a particulate film.

ACKNOWLEDGMENTS

H.L. acknowledges JSPS Kakenhi Startup Grant (Grant No. 21K20350). This work has benefited from a French State grant "BOGUS" ANR-19-CE06-0030-02. We are very thankful to Prof. Dillip K. Satapathy from IIT Madras for insightful discussions during the development of the project and for facilitating the preliminary experiments. H.L. also acknowledges Kazumasa A. Takeuchi from The University of Tokyo for frequent discussion.

-
- [1] P. Xu, A. Mujumdar, and B. Yu, Drying-induced cracks in thin film fabricated from colloidal dispersions, *Drying Technol.* **27**, 636 (2009).
- [2] A. F. Routh, Drying of thin colloidal films, *Rep. Prog. Phys.* **76**, 046603 (2013).
- [3] F. Giorgiutti-Dauphiné and L. Pauchard, Drying drops, *Eur. Phys. J. E* **41**, 32 (2018).
- [4] P. Bacchin, D. Brutin, A. Davaille, E. Di Giuseppe, X. D. Chen, I. Gergianakis, F. Giorgiutti-Dauphiné, L. Goehring, Y. Hallez, R. Heyd *et al.*, Drying colloidal systems: Laboratory models for a wide range of applications, *Eur. Phys. J. E* **41**, 94 (2018).
- [5] H. Lama, M. G. Basavaraj, and D. K. Satapathy, Desiccation cracks in dispersion of ellipsoids: Effect of aspect ratio and applied fields, *Phys. Rev. Mater.* **2**, 085602 (2018).
- [6] A. Sarkar and M. S. Tirumkudulu, Delamination of drying nanoparticle suspensions, *Soft Matter* **7**, 8816 (2011).
- [7] F. Giorgiutti-Dauphiné and L. Pauchard, Elapsed time for crack formation during drying, *Eur. Phys. J. E* **37**, 39 (2014).
- [8] F. Giorgiutti-Dauphiné and L. Pauchard, Dynamic delamination of drying colloidal films: Warping and creep behavior, *Colloids Surf., A* **466**, 203 (2015).
- [9] B. Yang, J. S. Sharp, and M. I. Smith, The interplay of crack hopping, delamination and interface failure in drying nanoparticle films, *Sci. Rep.* **6**, 32296 (2016).
- [10] H. Lama and R. Mondal, The physics of drying of colloidal dispersion: Pattern formation and desiccation cracks, *arXiv:2011.14029*.
- [11] R. W. Style, S. S. Peppin, and A. C. Cocks, Mud peeling and horizontal crack formation in drying clays, *J. Geophys. Res.* **116**, F01025 (2011).
- [12] L. Goehring, A. Nakahara, T. Dutta, S. Kitsunozaki, and S. Tarafdar, *Desiccation Cracks and Their Patterns: Formation and Modelling in Science and Nature* (Wiley, Hoboken, NJ, 2015).
- [13] L. Pauchard, F. Parisse, and C. Allain, Influence of salt content on crack patterns formed through colloidal suspension desiccation, *Phys. Rev. E* **59**, 3737 (1999).
- [14] K. B. Singh and M. S. Tirumkudulu, Cracking in Drying Colloidal Films, *Phys. Rev. Lett.* **98**, 218302 (2007).
- [15] A. L. R. Sibrant and L. Pauchard, Effect of the particle interactions on the structuration and mechanical strength of particulate materials, *Europhys. Lett.* **116**, 49002 (2016).
- [16] M. S. Tirumkudulu and W. B. Russel, Cracking in drying latex films, *Langmuir* **21**, 4938 (2005).
- [17] T. L. Anderson, *Fracture Mechanics: Fundamentals and Applications* (Taylor & Francis, New York, 2017).
- [18] S. Inasawa, Y. Oshimi, and H. Kamiya, Formation kinetics of particulate films in directional drying of a colloidal suspension, *Soft Matter* **12**, 6851 (2016).
- [19] A. Varshney, P. Sharma, A. Sane, S. Ghosh, and S. Bhattacharya, Desorption to Delamination: Dynamics of Detachment in a Colloidal Thin Film, *Phys. Rev. Lett.* **105**, 154301 (2010).
- [20] F. Boulogne and H. A. Stone, Self-crumpling elastomers: Bending induced by the drying stimulus of a nanoparticle suspension, *Europhys. Lett.* **108**, 19001 (2014).
- [21] A. Osman, L. Goehring, H. Stitt, and N. Shokri, Controlling the drying-induced peeling of colloidal films, *Soft Matter* **16**, 8345 (2020).
- [22] C. Brinker and G. Scherer, *Sol-Gel Science: The Physics and Chemistry of Sol-Gel Processing* (Academic, New York, 1990).
- [23] W. C. Oliver and G. M. Pharr, An improved technique for determining hardness and elastic modulus using load and

- displacement sensing indentation experiments, *J. Mater. Res.* **7**, 1564 (1992).
- [24] X. Ma, J. Lowensohn, and J. C. Burton, Universal scaling of polygonal desiccation crack patterns, *Phys. Rev. E* **99**, 012802 (2019).
- [25] J. P. Pantina and E. M. Furst, Elasticity and Critical Bending Moment of Model Colloidal Aggregates, *Phys. Rev. Lett.* **94**, 138301 (2005).
- [26] K. Kendall, N. M. Alford, and J. D. Birchall, Elasticity of particle assembles as a measure of the surface energy of solids, *Proc. R. Soc. London, Ser. A* **412**, 269 (1987).
- [27] S. Leroch and M. Wendland, Influence of capillary bridge formation onto the silica nanoparticle interaction studied by grand canonical Monte Carlo simulations, *Langmuir* **29**, 12410 (2013).
- [28] R. D. Deegan, Pattern formation in drying drops, *Phys. Rev. E* **61**, 475 (2000).
- [29] We assume that the particulate film's permeability k is not affected by the increasing salinity. However, adding salt in a colloidal dispersion increases the amorphous nature of the gel phase; the permeability is then slightly modified by the salt content.